A Closed-Form Robust Cluster-Analysis-Based Multibaseline InSAR Phase Unwrapping and Filtering Algorithm With Optimal Baseline Combination Analysis

Zhihui Yuan, *Member, IEEE*, Zhong Lu, *Senior Member, IEEE*, Lifu Chen, and Xuemin Xing

***Abstract*— Phase unwrapping (PU) and phase filtering are the key procedures for the interferometric synthetic aperture radar (InSAR) technology. As one of the most popular multibaseline PU (MBPU) algorithms, the cluster-analysis (CA)-based MBPU algorithm still has some problems that need to be improved. To begin with, the cluster ambiguity vector is obtained by searching the nearest integer point to the cluster centerline with known slope and intercept in the search space. It will be time-consuming and inconvenient when the number of baselines or the search space is too large. In addition, they do not have the capacity of phase filtering. Moreover, they do not consider the impact of different baseline combinations on the performance of the CA-based MBPU algorithm. For these reasons, a novel CA-based MBPU and filtering (MBPUF) algorithm is proposed in this article. The main contributions of this article are that it gives the closed-form solving formulas of the cluster ambiguity vector to improve the efficiency of the CA-based MBPU algorithm, proposes a novel MB InSAR phase-filtering strategy that makes the CA-based MBPU algorithm capable of solving the phase-discontinuity problem and improving the height-reconstruction accuracy simultaneously, and utilizes the optimal baseline combination to improve the robustness of the CA-based MBPU algorithm. Theoretical analysis and experiments on both simulated and real MB InSAR data sets show the effectiveness and robustness of the proposed closed-form robust CA-based MBPUF algorithm.**

***Index Terms*— Cluster analysis (CA), interferometric synthetic aperture radar (InSAR), multibaseline (MB), optimal baseline, phase filtering, phase unwrapping (PU).**

Manuscript received September 4, 2019; revised October 15, 2019 and November 7, 2019; accepted December 16, 2019. This work was supported in part by the National Natural Science Foundation of China under Grant 61701047, Grant 41701536, and Grant 61971071, in part by the Hunan Provincial Natural Science Foundation of China under Grant 2019JJ50639 and Grant 2017JJ3322, in part by the Scientific Research Fund of Hunan Provincial Education Department under Grant 18A148 and Grant 16B004, and in part by the China Scholarship Council under Grant 201800800006. *(Corresponding author: Zhihui Yuan.)*

Zhihui Yuan is with the Laboratory of Radar Remote Sensing Applications, School of Electrical and Information Engineering, Changsha University of Science and Technology, Changsha 410114, China, and also with the Roy M. Huffington Department of Earth Sciences, Southern Methodist University, Dallas, TX 75275 USA (e-mail: yuanzhihui@csust.edu.cn).

Zhong Lu is with the Roy M. Huffington Department of Earth Sciences, Southern Methodist University, Dallas, TX 75275 USA (e-mail: zhonglu@smu.edu).

Lifu Chen is with the Laboratory of Radar Remote Sensing Applications, School of Electrical and Information Engineering, Changsha University of Science and Technology, Changsha 410114, China (e-mail: lifu_chen@csust.edu.cn).

Xuemin Xing is with the School of Traffic and Transportation Engineering, Changsha University of Science and Technology, Changsha 410114, China (e-mail: xuemin.xing@csust.edu.cn).

Color versions of one or more of the figures in this article are available online at http://ieeexplore.ieee.org.

Digital Object Identifier 10.1109/TGRS.2019.2962001

I. Introduction

INTERFEROMETRIC synthetic aperture radar (InSAR) is the key technique for terrain height (also known as the digital elevation model, DEM) extraction and deformation monitoring with high spatial resolution and high measurement accuracy [1]–[3]. It takes the advantage of the fact that the ground elevation or the deformation amplitude is related to the absolute interferometric phase between the signals received by the two InSAR antennas. However, only the principal values of the absolute interferometric phase, modulo 2π, can be measured from the complex-valued resolution element. Therefore, a crucial processing procedure, phase unwrapping (PU), must be carried out to remove the modulo 2π ambiguity of the wrapped interferometric phase [4], [5].

As is known to all, the traditional single-baseline PU (SBPU) is an ill-posed inverse problem from the mathematical viewpoint [6], [7]. Because there are two unknowns (the integer ambiguity and the unwrapped phase), in one equation that will lead to many solutions. To ensure the uniqueness of the solution, SBPU assumes that the actual phase jumps between adjacent pixels are less than π. This assumption is called phase-continuity assumption or Itoh condition [8]. Unfortunately, not all situations satisfy this assumption in practice because of complex terrain or severe deformation. Thus, a new kind of technique, multifrequency, and/or multibaseline PU (MFPU and/or MBPU), has been proposed to eliminate the phase-continuity assumption [9]. Since the principles of MBPU and MFPU are essentially the same, and MB InSAR is more common in the practical applications, only MBPU is discussed in this article for the sake of simplicity. Essentially, the elimination of the phase-continuity assumption means the extension of the ambiguity phase interval or the ambiguity height interval because of the baseline diversity.

Over the past two decades, MBPU has been extensively investigated for height estimation [10], [11] and deformation estimation [12]–[16]. According to the difference of

the wrapped phase processing, the MBPU methods can be roughly divided into two categories: statistical estimation methods [17]–[30] and nonstatistical estimation methods [9], [31]–[41]. For the statistical estimation methods, the height [17]–[20], [22]–[30] or height difference [21] of the terrain is regarded as a parameter to be estimated in a statistical distribution framework, which is modeled by the probability density function of the interferometric phase [42], [43]. And the parameter is estimated by the maximum likelihood (ML) [17]–[22], [25], [26] or the maximum *a posteriori* (MAP) [23], [24], [27] criteria. For the nonstatistical estimation method, the combined information of multiple InSAR interferograms with different baseline lengths is directly used to estimate the absolute phase without using the probability density function of the interferometric phase.

The development of the two categories of MBPU methods mentioned above can be divided into three stages. In the first stage, the Chinese remainder theorem (CRT) method, the projection method, and the linear combination method are first proposed to facilitate the independent PU of each pixel [9]. At the same time, two classes of MBPU methods are introduced in [17]: the first is based on the robust weighted or unweighted least-squares PU method proposed for SBPU, whereas the second attacks the problem in an ML formulation. In [18]–[21], other similar methods based on ML estimation are presented. In [31], a coarse-to-fine iterative method is proposed to unwrap the wrapped interferogram with a longer baseline from the unwrapped interferogram with a shorter baseline. In [32], the Kalman filtering (KF) technique is first applied to MBPU. However, all the previously mentioned methods have a serious issue, i.e., they are very sensitive to noise, and small phase noise may cause a large PU error. So, in the second stage, some extra measures to improve the noise robustness of the MBPU methods have been made. For the statistical estimation methods, local plane hypothesis is used to approximate the unknown surface in the ML estimation [22], and the *a priori* distribution of the unknown terrain height is modeled to help the MAP estimation [23], [24]. In [28], the DEM-reconstruction accuracy of the ML and MAP estimation methods is analyzed. In [29], a good review on the ML and MAP estimation methods for the DEM reconstruction is showed in detail. More than that, the MAP estimation method has been applied to the multichannel spaceborne/stationary SAR interferometry [30]. For the nonstatistical estimation method, an improved closed-form CRT-based technique [33] is designed to improve the performance of the traditional CRT-based MBPU method proposed in [9]. In addition, another kind of MBPU method, the robust cluster analysis (CA) based method and its extensions and improvements, has been proposed in [34]–[36]. In the CA-based MBPU method, all pixels are divided into different clusters according to the combined information of multiple interferograms, and then each cluster center's information is used for MBPU. In the third stage, filtering techniques and SBPU techniques are widely applied to MBPU for further reducing the effects of phase noise. The application of the filtering technique makes MBPU capable of PU and phase filtering at the same time. In [25] and [26], ML criteria and extended Kalman filter (EKF) are combined to build the multichannel EKF PU framework, achieving interesting performance improvements. In [27], the nonlocal filtering technique is introduced into the MAP-based MBPU method. For the nonstatistical estimation method, traditional SBPU techniques have been extended to MBPU. Inspired by the thought of [21], Yu and Lan [37] proposed a two-stage programming approach (TSPA) to transplant the framework of SBPU and the two key concepts used in SBPU (residue and branch cut) into MBPU. From then on, the research related to TSPA has developed rapidly. In [38], the local plane model is embedded into TSPA for improving the robustness of the MBPU algorithm. In [39], unscented Kalman filter is integrated into the TSPA framework. In [40], the SBPU-max-flow (PUMA) algorithm has been extended to MBPU to improve the robustness of the MBPU algorithm. In [41], a technique for applying the TSPA-based MBPU method to large-scale (LS) MB InSAR data sets has been put forward. As TSPA attracts more and more attention, researchers start to jointly call all the TSPA-related techniques as TSPAInSAR. It is worth noticing that the three KF-based MBPU methods proposed in [44]–[46] do not consider the phase-discontinuity problem, and thus their application scope is limited.

In this article, we propose a novel closed-form robust CA-based MBPU and filtering (MBPUF) algorithm and analyze the condition of optimal baseline combination. There are three differences between the proposed method and the previous CA-based MBPU methods. First, in the previous CA-based MBPU methods, the cluster ambiguity vector (the term will be defined in Section II) is obtained by searching the nearest integer point to the cluster centerline with known slope and intercept in the search space. It will be time-consuming and inconvenient when the number of baselines or the search space is too large. In this article, we provide the closed-form solution of the cluster ambiguity vector, which is helpful to improve the efficiency of the CA-based MBPU algorithm. Second, we propose a novel cluster phase-filtering strategy, which allows the CA-based MBPU method to simultaneously solve the phase-discontinuity problem and improve the height-reconstruction accuracy like the other KF-based MBPU methods. Third, we analyze the impact of different baseline combinations on the MBPU algorithm and give the conditions of the optimal baseline combination required by MBPU. It is helpful to improve the robustness of the MBPU algorithm and can provide guidance for the baseline combination design of actual MB InSAR system. To reconstruct the terrain height by the unwrapped phase, the clustering algorithm proposed in [34]–[36] is first used to distinguish different clusters; thereafter, the closed-form solution formula is used to calculate the cluster ambiguity vector of each cluster; and then, the proposed cluster phase-filtering method is used to filter the original wrapped phase; after that, the unwrapped phase is obtained according to the cluster ambiguity vector and the filtered wrapped phase; at last, the terrain height is reconstructed by the unwrapped phase and other MB InSAR system parameters.

The rest of this article is organized as follows. In Section II, the principle of the CA-based MBPU method is reviewed and

the disadvantage of this method is analyzed. In Section III, the novel closed-form robust CA-based MBPUF algorithm is described in detail. Three experiments with both simulated and real MB InSAR data sets are presented in Section IV to verify the effectiveness of the proposed method. Finally, some conclusions are drawn in Section V.

II. Review of CA-Based MBPU Method and Problem Analysis

For a pixel, considering an MB InSAR system with a working wavelength λ, a view angle (or look angle) θ, and a normal baseline (or a perpendicular baseline) $B_i (i = 1, 2, \ldots, N)$, the terrain height of the sth pixel can be expressed as follows [37]:

$$h(s) = \frac{\lambda \cdot r(s) \cdot \sin\theta}{4\pi \cdot B_i} \cdot \psi_i(s) \tag{1}$$

where $r(s)$ is the slant range of the sth pixel between the master antenna and the target point, and $\psi_i(s)$ is the flattened absolute interferometric phase of the sth pixel in the ith interferogram. The term "flattened" means that the flat earth phase [2] has been removed. So, the ambiguity height (the height resulting in a phase change of one fringe, i.e., 2π) [2], [3] of the ith interferogram is obtained by

$$H_i = \frac{\lambda \cdot r(s) \cdot \sin\theta}{2B_i}. \tag{2}$$

However, only the so-named wrapped interferometric phase (from 0 to 2π or $-\pi$ to π) can be directly measured by the InSAR system. It can be expressed as follows:

$$\varphi_i(s) = \psi_i(s) - k_i(s) \cdot 2\pi \tag{3}$$

where $k_i(s)$ is the unknown integer ambiguity of the sth pixel in the ith interferogram. We can see from (3) that $k_i(s)$ must be recovered if we want to obtain the absolute interferometric phase $\psi_i(s)$. And then $\psi_i(s)$ can be converted to the terrain height $h(s)$ by (1) directly. Obviously, $\psi_i(s)$ and $k_i(s)$ cannot be solved simultaneously with (3) because there are two unknowns but only one equation.

There are two ways to solve (3). The first method is to use the traditional single-baseline InSAR PU technology, SBPU, mentioned in Section I, which is an ill-posed inverse problem because of the requirement of the phase-continuity assumption (i.e., the differences of the absolute interferometric phase between adjacent pixels are less than π). The second is to use the MB PU technology, MBPU, which will be used in this article. For simplicity, let us assume that there are only two baselines in the MB InSAR system. Then we can obtain the relationship of the two interferograms by combining (1)–(3), i.e.,

$$\frac{\varphi_1(s)+k_1(s)\cdot 2\pi}{B_1} = \frac{\varphi_2(s)+k_2(s)\cdot 2\pi}{B_2} = \frac{4\pi}{\lambda \cdot r(s)\cdot \sin\theta}\cdot h(s). \tag{4}$$

It should be noted that the equal sign is only valid when there is no deformation during the measurement, i.e., only the elevation exists. If we take $k_1(s)$ as an independent variable and $k_2(s)$ as a dependent variable, (4) can be transformed into a linear equation as follows:

$$k_2(s) = \frac{B_2}{B_1} \cdot k_1(s) + \frac{B_2 \cdot \varphi_1(s) - B_1 \cdot \varphi_2(s)}{2\pi \cdot B_1}. \tag{5}$$

According to (5) and related definitions,we known that the slope of the straight line is a constant, B_2/B_1, and the intercept of the straight line is determined by B_1, B_2, $\varphi_1(s)$ and $\varphi_2(s)$ simultaneously [please refer to the second term on the right side of (5)]. If we define the term ambiguity vector $[k_1(s), k_2(s)]$ to represent the integer ambiguity of the sth pixel in the two interferograms, the pixels with the same ambiguity vector can be considered to belong to the same cluster. We refer to the ambiguity vector corresponding to the pixels belonging to the same cluster as the cluster ambiguity vector. In addition, the straight lines corresponding to these pixels have the same slope, B_2/B_1, and pass though the same integer point (K_1, K_2) on the k_1–k_2 plane (as shown in Fig. 1). Therefore, we could get a conclusion that all straight lines with the same ambiguity vector have the same intercept, i.e., they are overlapping. In other words, all pixels whose corresponding straight lines have the same intercept can be grouped into the same cluster. It is the essence of the CA-based MBPU algorithm.

However, the measured intercept often deviates from its corresponding true intercept owing to the influence of phase noise. To reduce this influence, two different clustering strategies are proposed. Yu *et al.* [34] use the intercept information to distinguish different clusters and to determine the corresponding cluster ambiguity vector by finding the peak of the intercept statistical histogram curve. Liu *et al.* [35] combine the intercept and spatial location information together to distinguish different clusters, which is named density-based clustering algorithm. Detailed descriptions of these two strategies can be found in [34] and [35].

Although the performance of these two methods is better than the traditional pixel to pixel's CRT-based MBPU method, many further improvements can still be made. First, the cluster ambiguity vector is obtained by searching the nearest integer point to the cluster centerline with the known slope and intercept in the search space. It will be time-consuming and inconvenient when the number of baselines or search space is too large. Second, they do not have the capacity of phase filtering like the KF-based MBPU method. Third, they do not consider the impact of different baseline combinations on the performance of the CA-based MBPU algorithm. For these reasons, this article improves the CA-based MBPU algorithm from three different aspects. A detailed description of these improvements will be presented in the following section.

III. Closed-Form Robust CA-Based MBPUF Algorithm

According to the analysis of Section II, a closed-form robust CA-based MBPUF algorithm is proposed in this section. For the sake of simplicity, we describe the design and analysis of the algorithm in the case of two baselines at first (we refer to it as dual-baseline PU, DBPU). Then we will discuss its generalization to the MB case.

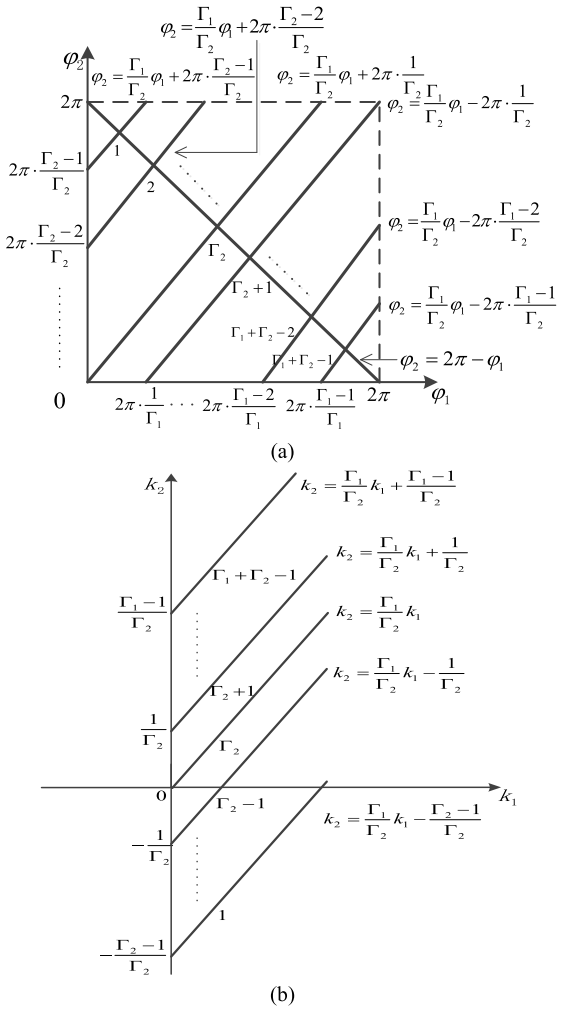

Fig. 1. Relationship between (a) wrapped phases φ_1 and φ_2 and (b) ambiguity numbers k_1 and k_2.

A. Closed-Form Solution of Cluster Ambiguity Vector

We all know that the ambiguity height can be obtained by (2) based on the baseline information and other InSAR system parameters. In general, the baseline length is obtained by measurement or estimation, which should be a rational number, and the corresponding ambiguity height (H_1 or H_2) is, of course, a rational number, so the baseline ratio must also be a rational number. Therefore, H_1 and H_2 can be decomposed into a form of multiplying a common factor and an integer as shown below by the method of finding the greatest common divisor:

$$\begin{cases} H_1 = M \cdot \Gamma_1 \\ H_2 = M \cdot \Gamma_2 \end{cases} \tag{6}$$

where M is the common factor, Γ_1 and Γ_2 are the positive integers and they are coprime. The decomposition process is as follows: when H_1 and H_2 are integers, then M is equal to the greatest common divisor of H_1 and H_2, i.e., gcd (H_1, H_2); when both H_1 and H_2 are decimal, then the same number of decimal places is reserved (assuming n decimal places are reserved), and M = gcd ($H_1 * 10^n$, $H_2 * 10^n$)/10^n. For example, if $H_1 = 13.8$ and $H_2 = 32.2$, then M = gcd (13.8 × 10, 32.2 × 10)/10 = 4.6, $\Gamma_1 = 13.8/4.6 = 3$, and $\Gamma_2 = 32.2/4.6 = 7$.

Then, according to (1)–(3) and (6), we can obtain

$$\frac{h(s)}{M} = k_1(s)\cdot\Gamma_1 + \frac{\varphi_1(s)}{2\pi}\cdot\Gamma_1 = k_2(s)\cdot\Gamma_2 + \frac{\varphi_2(s)}{2\pi}\cdot\Gamma_2. \tag{7}$$

Suppose that $\varphi_{1,2}(s) \in [0, 2\pi)$, and define

$$\begin{cases} q_i(s) = \left\lfloor \dfrac{\varphi_i(s)}{2\pi}\cdot\Gamma_i \right\rfloor \\ r_i(s) = \left\{ \dfrac{\varphi_i(s)}{2\pi}\cdot\Gamma_i \right\}, \end{cases} \quad i = 1, 2 \tag{8}$$

where $\lfloor\cdot\rfloor$ and $\{\cdot\}$ represent the integer and decimal parts of a real number, respectively. Then, we can obtain the linear congruence equations from (7) as follows:

$$\begin{cases} \left\lfloor \dfrac{h(s)}{M} \right\rfloor = k_1(s)\Gamma_1 + q_1(s) \\ \left\lfloor \dfrac{h(s)}{M} \right\rfloor = k_2(s)\Gamma_2 + q_2(s) \end{cases} \tag{9}$$

where $\lfloor h(s)/M \rfloor$ is the integer solution of the congruence equations to be solved, $k_i(s)$ is the unknown ambiguity number of the ambiguity vector $[k_1(s), k_2(s)]$, Γ_i is the known modulus in (6), $q_i(s)$ is the known remainder calculated by (8), and the dependence of them on s is understood. Corresponding to the ambiguity vector, the remainder vector is defined as $[q_1(s), q_2(s)]$. Obviously, $\lfloor h(s)/M \rfloor$ can be solved by CRT [33], [48]. If we define

$$\Gamma = \Gamma_1 \cdot \Gamma_2 \tag{10}$$

$$\gamma_i = \Gamma/\Gamma_i, \quad i = 1, 2 \tag{11}$$

then, according to the classical CRT formula, $\lfloor h(s)/M \rfloor$ can be uniquely solved out in the interval $0, \Gamma)$ [48], i.e.,

$$\left\lfloor \frac{h(s)}{M} \right\rfloor = \sum_{i=1}^{2} \bar{\gamma}_i \gamma_i q_i(s) (\mathrm{mod}\,\Gamma) \tag{12}$$

where $\bar{\gamma}_i$ is the modular multiplicative inverse of γ_i modulo Γ_i. $\bar{\gamma}_i$ is actually the smallest integer solution of x in the indefinite equation $x\gamma_i + y\Gamma_i = \gcd(\gamma_i, \Gamma_i) = 1$. It can be calculated by the extended Euclidean algorithm, and the relevant codes can be obtained through the Web. The relationship between them is as follows:

$$\bar{\gamma}_i \gamma_i \equiv 1 (\mathrm{mod}\,\Gamma_i), \quad i = 1, 2. \tag{13}$$

Since $\lfloor h(s)/M \rfloor$ has been solved now, the closed-form solution of the ambiguity vector can be obtained by

$$k_i(s) = \left(\left\lfloor \frac{h(s)}{M} \right\rfloor - q_i(s) \right) / \Gamma_i, \quad i = 1, 2. \tag{14}$$

If we use (8) directly to calculate $q_i(s)$ according to the noisy wrapped interferometric phase $\hat{\varphi}_i(s)$, it will belong to the traditional pixel to pixel's CRT-based MBPU method, which has been proven to be not robust to noise [9]. In the CA-based MBPU method, we will calculate $q_i(s)$ according

to the intercept of the cluster's centerline. Then we can see from (2) and (6) that

$$\frac{B_2}{B_1} = \frac{H_1}{H_2} = \frac{\Gamma_1}{\Gamma_2}. \tag{15}$$

And the intercept of the straight line corresponding to the pixel s can be expressed as follows:

$$\begin{aligned}\text{intercept}_{12}(s) &= \frac{1}{2\pi} \cdot \left(\frac{\Gamma_1}{\Gamma_2} \cdot \varphi_1(s) - \varphi_2(s) \right) \\ &= k_2(s) - \frac{\Gamma_1}{\Gamma_2} \cdot k_1(s). \end{aligned} \tag{16}$$

If we take $\varphi_1(s)$ as the independent variable and $\varphi_2(s)$ as the dependent variable, then the following linear equation can be obtained from (16):

$$\begin{aligned}\varphi_2(s) &= \frac{\Gamma_1}{\Gamma_2} \cdot \varphi_1(s) + 2\pi \cdot \left(\frac{\Gamma_1}{\Gamma_2} \cdot k_1(s) - k_2(s) \right) \\ &= \frac{\Gamma_1}{\Gamma_2} \cdot \varphi_1(s) - 2\pi \cdot \text{intercept}_{12}(s). \end{aligned} \tag{17}$$

Obviously, different $\text{intercept}_{12}(s)$ corresponds to a different straight line on the $\varphi_1 - \varphi_2$ plane too, and each straight line is "folded" into the square area of $\varphi_{1,2}(s) \in [0, 2\pi)$ (as shown in Fig. 1). Furthermore, because Γ_1 and Γ_2 are coprime, the $\Gamma_1 + \Gamma_2 - 1$ line segments can be obtained in total. Therefore, we can know that the value of each $\text{intercept}_{12}(s)$ will be limited to $(-1, \Gamma_1/\Gamma_2)$. What is more, it can be seen from the second expression of (16) that, since $k_i(s)$ and Γ_i are the integers, the value of each $\text{intercept}_{12}(s)$ can only be an element of the following set:

$$S = \left\{ -\frac{\Gamma_2 1}{\Gamma_2}, -\frac{\Gamma_2 2}{\Gamma_2}, \ldots, 0, \ldots, \frac{\Gamma_1 2}{\Gamma_2}, \frac{\Gamma_1 1}{\Gamma_2} \right\}. \tag{18}$$

However, the intercept may deviate from its true value owing to the existence of phase noise, so the corresponding ambiguity vector cannot be directly calculated by the intercept of each pixel. Instead, we choose the intercept in S that is nearest to the intercept of each cluster's centerline as the true intercept of the cluster, which is named the cluster intercept in this article. Consequently, the value of the cluster intercept can only be an element of the set S for the InSAR system with two baselines.

From (5) and (17), the relationship between the wrapped phases φ_1 and φ_2, and ambiguity numbers k_1 and k_2 can be shown in Fig. 1 (suppose $B_2 > B_1$). As can be seen from Fig. 1(a), the points on the same line segment correspond to the same ambiguity vector, i.e., the same cluster. And the corresponding relationship between the ambiguity vector and the remainder vector is one-to-many or one-to-one. Therefore, any point on the line segment can be selected to calculate its corresponding remainder vector, and then the corresponding cluster ambiguity vector can be obtained based on the remainder vector and other known information. To obtain the closed-form coordinate formula of the point, we select the intersection point of the line segment with the following straight line that goes through points $(0, 2\pi)$ and $(2\pi, 0)$ as the cluster central point to calculate the remainder vector, which is named the cluster central point remainder:

$$\varphi_2 = 2\pi - \varphi_1. \tag{19}$$

Then the following coordinate formulas of the cluster central point can be obtained by solving (17) and (19) simultaneously:

$$\begin{cases} \varphi_1(l) = \dfrac{2\pi \cdot \Gamma_2 \cdot (1 + \text{intercept}_{12}(l))}{\Gamma_1 + \Gamma_2} \\ \varphi_2(l) = \dfrac{2\pi \cdot (\Gamma_1 - \Gamma_2 \cdot \text{intercept}_{12}(l))}{\Gamma_1 + \Gamma_2}, \end{cases} \quad l = 1, 2, \ldots, \Gamma_1 + \Gamma_2 - 1 \tag{20}$$

where $\text{intercept}_{12}(l)$ is the cluster intercept of the lth cluster and $[\varphi_1(l), \varphi_2(l)]$ is named the cluster central point phase vector in this article. It must be reminded that the pixel index s has been replaced with the cluster index l in (20), because at this time, we assume that there are many pixels in the same cluster, and the ambiguity vectors of the pixels belonging to the same cluster are all the same, i.e., the cluster ambiguity vector, which only needs to be solved once. If $\varphi_i(l)$ is substituted to (8) for calculating the cluster central point remainder $q_i(l)$, then the closed-form solution of the cluster ambiguity vector of the lth cluster can be obtained by (14)

$$q_i(l) = \left\lfloor \frac{\varphi_i(l)}{2\pi} \cdot \Gamma_i \right\rfloor \tag{21}$$

$$\left\lfloor \frac{h(l)}{M} \right\rfloor = \sum_{i=1}^{2} \bar{\gamma}_i \gamma_i q_i(l) (\text{mod} \Gamma) \tag{22}$$

$$k_i(l) = \left(\left\lfloor \frac{h(l)}{M} \right\rfloor - q_i(l) \right) / \Gamma_i, \quad i = 1, 2. \tag{23}$$

B. Cluster Phase Filtering

In fact, MBPU technique also has the capacity of phase filtering. It can be partially realized by projecting the noisy phase onto the straight-line segment that belong to its corresponding cluster. As mentioned in the previous section, we know from Fig. 1(a) that the points on the same line segment correspond to the same cluster. However, owing to the influence of phase noise, the measured wrapped interferometric phase vector points $[\hat{\varphi}_1(s), \hat{\varphi}_2(s)]$ corresponding to the same cluster may not fall onto the cluster's line segment, but distribute into the whole $2\pi \times 2\pi$ square region in the $\varphi_1 - \varphi_2$ coordinate system. Therefore, we can project the noisy phase vector point $[\hat{\varphi}_1(s), \hat{\varphi}_2(s)]$ onto the cluster's line segment to achieve the result of phase filtering. This kind of phase-filtering method is named cluster phase filtering in this article. Obviously, the most intuitive way of the projection is perpendicular projection, which takes the intersection obtained by projecting the noisy phase vector point $[\hat{\varphi}_1(s), \hat{\varphi}_2(s)]$ perpendicularly onto the cluster's line segment as the filtered phase vector point $[\bar{\varphi}_1(s), \bar{\varphi}_2(s)]$ [please refer to Fig. 2(a)]. They can be expressed as follows:

$$\begin{cases} \bar{\varphi}_1(s) = \dfrac{\Gamma_1 \cdot \Gamma_2}{\Gamma_1^2 + \Gamma_2^2} \left(\hat{\varphi}_2(s) + \dfrac{\Gamma_2}{\Gamma_1} \hat{\varphi}_1(s) + 2\pi \cdot \text{intercept}_{12}(l) \right) \\ \bar{\varphi}_2(s) = \dfrac{\Gamma_1^2}{\Gamma_1^2 + \Gamma_2^2} \left(\hat{\varphi}_2(s) + \dfrac{\Gamma_2}{\Gamma_1} \hat{\varphi}_1(s) \right) - \dfrac{2\pi \cdot \Gamma_2^2 \cdot \text{intercept}_{12}(l)}{\Gamma_1^2 + \Gamma_2^2}. \end{cases} \tag{24}$$

Of course, other projection methods can also be used. In fact, we can take the intersection of the straight line passing through

$[\hat{\varphi}_1(s),\ \hat{\varphi}_2(s)]$ with the arbitrary slope and the cluster line segment as the filtered phase vector point $[\bar{\varphi}_1(s),\ \bar{\varphi}_2(s)]$. However, different slopes will lead to different phase-filtering results. For example, if $\hat{\varphi}_2(s)$ is far more reliable than $\hat{\varphi}_1(s)$, then we can choose the horizontal projection as shown in Fig. 2(b) to obtain the best phase-filtering result. On the contrary, if $\hat{\varphi}_1(s)$ is far more reliable than $\hat{\varphi}_2(s)$, we can choose the vertical projection as shown in Fig. 2(c) to obtain the best phase-filtering result. Therefore, we can determine the slope of the straight line according to the coherence of the two interferograms. Suppose that the coherence coefficients of the two interferograms are γ_1 and γ_2, respectively. Then the slope of the straight line can be set to be $-|\gamma_1|/|\gamma_2|$, where $|\cdot|$ represents the absolute value. Thus, the equations of the two straight lines can be expressed as follows:

$$\begin{cases} \varphi_2 = -\dfrac{|\gamma_1|}{|\gamma_2|}\varphi_1 + \hat{\varphi}_2(s) + \dfrac{|\gamma_1|}{|\gamma_2|}\hat{\varphi}_1(s) \\ \varphi_2 = \dfrac{\Gamma_1}{\Gamma_2}\varphi_1 - 2\pi \cdot \text{intercept}_{12}(l). \end{cases} \tag{25}$$

Solving the equations, the filtered phase vector point $[\bar{\varphi}_1(s), \bar{\varphi}_2(s)]$ can be obtained as follows:

$$\begin{cases} \bar{\varphi}_1(s) = \dfrac{\Gamma_2|\gamma_2|}{\Gamma_1|\gamma_2| + \Gamma_2|\gamma_1|} \\ \times \left[\hat{\varphi}_2(s) + \dfrac{|\gamma_1|}{|\gamma_2|}\hat{\varphi}_1(s) + 2\pi \cdot \text{intercept}_{12}(l)\right] \\ \bar{\varphi}_2(s) = \dfrac{\Gamma_1|\gamma_2|}{\Gamma_1|\gamma_2| + \Gamma_2|\gamma_1|} \\ \times \left[\hat{\varphi}_2(s) + \dfrac{|\gamma_1|}{|\gamma_2|}\hat{\varphi}_1(s) - \dfrac{\Gamma_2|\gamma_1|}{\Gamma_1|\gamma_2|} \cdot 2\pi \cdot \text{intercept}_{12}(l)\right]. \end{cases} \tag{26}$$

At this point, we can see that the projections, as shown in Fig. 2, are the cases where $|\gamma_1|/|\gamma_2|$ takes three different special values. When $|\gamma_1|/|\gamma_2| = \Gamma_2/\Gamma_1$, the perpendicular projection shown in Fig. 2(a) is used; when $|\gamma_1|/|\gamma_2| = 0$, the horizontal projection shown in Fig. 2(b) is used; and when $|\gamma_1|/|\gamma_2| = \infty$, the vertical projection shown in Fig. 2(c) is used.

Another issue that needs special attention is that if the value of $\bar{\varphi}_i(s)$ is outside the defined range $[0, 2\pi)$ after projection, it should be wrapped into this range.

C. Optimal Baseline Combination

The robustness of the CA-based MBPU algorithm can also be improved by choosing the optimal baseline combination. A nonlinear mixed-integer programming-based baseline design criterion (referred to as the NIP criterion) has been proposed in [47] to maximize the measurement bias tolerance of the DBPU methods. According to the NIP criterion, the optimality condition for the CA-based DBPU method is [47]

$$\frac{B_2}{B_1} \geq W_2 + 1 \tag{27}$$

where W_2 is the number of ambiguities in an area with continuous ambiguity change of the longer baseline B_2's interferogram. It is actually the size of the search window for searching the solution of k_2. And $B_i (i = 1, 2)$ should satisfy the DB CRT condition [47] on each pixel. However, this

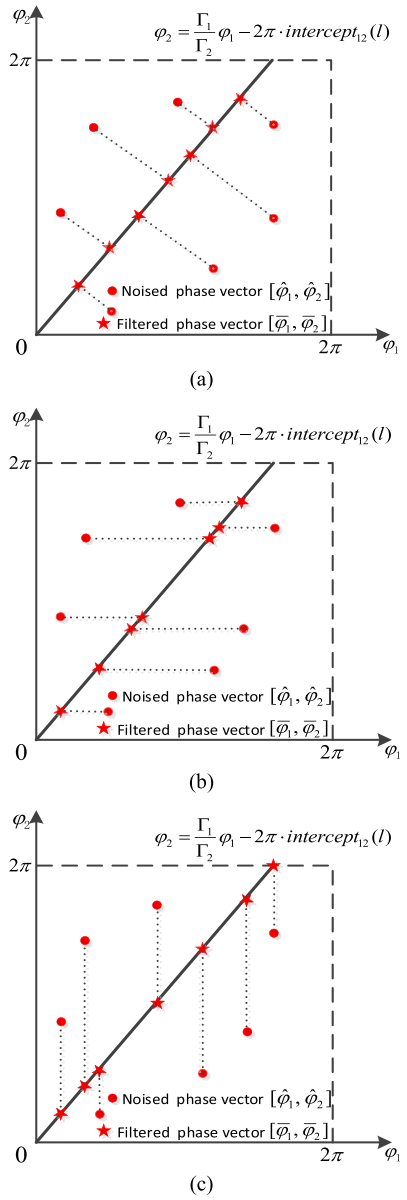

Fig. 2. Schematic illustration of cluster phase filtering. (a) Perpendicular projection when $|\gamma_1|/|\gamma_2| = \Gamma_2/\Gamma_1$. (b) Horizontal projection when $|\gamma_1|/|\gamma_2| = 0$. (c) Vertical projection when $|\gamma_1|/|\gamma_2| = \infty$.

condition only gives the lower limit of the optimal baseline combination B_2/B_1 but does not provide the upper limit. Obviously, the ratio of B_2/B_1 cannot be equal to infinity, and there must be an upper limit. Therefore, it is necessary to analyze its upper limit to narrow the selection range of the optimal baseline combination.

According to the closed-form robust CRT [33], [48] and the analysis in Section III-A, we know that $h(s)$ can be uniquely reconstructed in the interval from 0 to $M\Gamma$, which is named the total ambiguity height H_{total} in this article. It can be expressed as follows:

$$\begin{aligned} H_{\text{total}} &= M\Gamma = M\Gamma_1\Gamma_2 \\ &= \frac{M\Gamma_1 \cdot M\Gamma_2}{M} \\ &= \frac{1}{M} \cdot \left(\frac{\lambda \cdot r(s) \cdot \sin\theta}{2}\right)^2 \cdot \frac{1}{B_1 \cdot B_2}. \end{aligned} \tag{28}$$

Obviously, to guarantee the uniqueness of the reconstructed height, the maximum terrain height $h_{\max}$ of the target terrain cannot exceed the total ambiguity height, so we have

$$\frac{1}{M}\cdot\left(\frac{\lambda\cdot r(s)\cdot\sin\theta}{2}\right)^2\cdot\frac{1}{B_1\cdot B_2}>h_{\max} \tag{29}$$

i.e.,

$$B_1\cdot B_2<\frac{1}{M}\cdot\left(\frac{\lambda\cdot r(s)\cdot\sin\theta}{2}\right)^2\cdot\frac{1}{h_{\max}}. \tag{30}$$

What is more, from the analysis in [36], the increase of the ambiguity height of each interferogram can avoid some real clusters being incorrectly merged into adjacent clusters and improve the robustness of the CA-based MBPU algorithm. Therefore, it does not mean that the higher baseline ratio B_2/B_1 renders a better result. On the contrary, under the preconditions that (27) and (30) are satisfied, the length of B_2 should be as close as possible to B_1, which is the optimal condition that meets the optimal baseline combination.

D. Description of the Closed-Form Robust CA-Based DBPU and Filtering Algorithm

Under the conditions of optimal baseline combination, the closed-form robust CA-based DBPU and filtering algorithm can be depicted by the following 10 steps.

Step 1: Use the clustering method proposed in [34] or [35] to distinguish different clusters by considering the intercept, row, and line information of each pixel together. Then the number of clusters L and the intercept of each cluster's centerline are obtained.

Step 2: Find the cluster intercept $\text{intercept}_{12}(l)$ of each cluster for $l=1,2,\ldots,L$.

Step 3: Calculate the cluster central point phase vector $[\varphi_1(l),\ \varphi_2(l)]$ of each cluster according to (20).

Step 4: Calculate the cluster central point remainder vector $[q_1(l), q_2(l)]$ of each cluster according to (21).

Step 5: Calculate the integer solution $\lfloor h(l)/M\rfloor$ of the congruence equation (9) according to (22).

Step 6: Calculate the cluster ambiguity vector $[k_1(l), k_2(l)]$ of each cluster according to (23).

Step 7: Calculate the pixel ambiguity vector $[k_1(s), k_2(s)]$ of each pixel according to the clustering result of Step 1. That is to say, if pixel s belongs to the lth cluster, then we will make $[k_1(s), k_2(s)]=[k_1(l), k_2(l)]$.

Step 8: Calculate the filtered phase vector $[\bar{\varphi}_1(s),\ \bar{\varphi}_2(s)]$ of each pixel according to (26).

Step 9: Recover the unwrapped phase of each interferogram according to (3).

Step 10: Reconstruct the terrain height of all pixels according to (1).

For example, assume that $B_2/B_1=\Gamma_1/\Gamma_2=5/3$, the the relationship between the wrapped phases φ_1 and φ_2, and ambiguity numbers k_1 and k_2 can be shown in Fig. 3. If the intercept of a cluster's centerline is 5/7 after clustering, then we can know that its corresponding *cluster intercept* is 2/3. So from (20), we know that the cluster central point phase vector is $[\varphi_1(l),\ \varphi_2(l)]=[5\pi/4, 3\pi/4]$. Substituting them into (21) yields $[q_1(l),\ q_2(l)]=[3,\ 1]$. Then $\lfloor h(l)/M\rfloor$ can be uniquely solved out to be 13 by (22), and the cluster ambiguity vector will be $[k_1(l),\ k_2(l)]=[2,\ 4]$ by (23). In the same way, we can calculate all the cluster ambiguity vectors corresponding to all the cluster intercepts. According to the analysis of Section III-A, the total number of line segments is 7. And the corresponding relationship between the cluster intercept $\text{intercept}_{12}(l)$ and the cluster ambiguity vector $[k_1(l), k_2(l)]$ is shown in Fig. 4.

As can be seen from this example, if $B_2/B_1=\Gamma_1/\Gamma_2$ is known, then all the cluster ambiguity vectors corresponding to

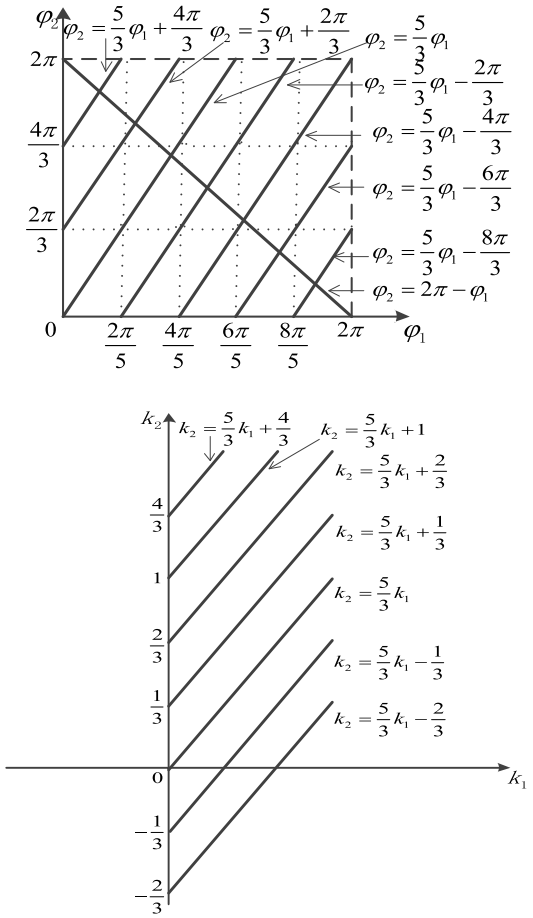

Fig. 3. Relationship between (a) wrapped phases φ_1 and φ_2 and (b) ambiguity numbers k_1 and k_2.

$$\begin{matrix}\textit{intercept}_{12}(l)\\ \begin{pmatrix}4/3\\1\\2/3\\1/3\\0\\-1/3\\-2/3\end{pmatrix}\end{matrix}\quad\Leftrightarrow\quad\begin{matrix}[k_1(l),k_2(l)]\\ \begin{pmatrix}[1,\ 3]\\[0,\ 1]\\[2,\ 4]\\[1,\ 2]\\[0,\ 0]\\[2,\ 3]\\[1,\ 1]\end{pmatrix}\end{matrix}$$

Fig. 4. Relationship between the cluster intercept $\text{intercept}_{12}(l)$ and the cluster ambiguity vector $[k_1(l), k_2(l)]$.

all the cluster intercepts can be calculated in advance, and then we can directly find the cluster ambiguity vector corresponding to a cluster by looking up the comparison table like Fig. 4. In this case, steps 3–7 can be omitted.

E. Generalization for the MB InSAR Case

The closed-form robust CA-based DBPU and filtering algorithm can be easily extended to MB cases. For MBPU, (7) can be extended to

$$k_1(l)\Gamma_1 + \frac{\varphi_1(l)}{2\pi}\Gamma_1 = k_2(l)\Gamma_2 + \frac{\varphi_2(l)}{2\pi}\Gamma_2 = \cdots = k_N(l)\Gamma_N + \frac{\varphi_N(l)}{2\pi}\Gamma_N. \quad (31)$$

And the value range of the subscript i in all the previous formulas will be from 1 to N. The straight lines in the previous 2-D plane will become the spatial straight lines in the N-dimensional space. Compared with the CA-based DBPU algorithm, there is almost no difference, except for the spatial dimensions where the algorithm performs. After the clustering result is obtained by the procedures described in [34] or [35], the unwrapped phase can be recovered cluster by cluster according to steps 2–9 of Section III-D.

IV. Performance Analysis

In this section, three experiments on the simulated and real InSAR data are used to test the performance of the proposed closed-form robust CA-based MBPUF method. The first experiment verifies the feasibility and effectiveness of the proposed MBPUF method on a simplified profile, especially the validity of the cluster phase filtering. The second experiment verifies the reliability of optimal baseline combination in improving the noise robustness of the MBPU method on a more realistic profile. The third experiment tests the performance of the method on a real MB InSAR data set. The first and third experiments will give a comparison of the results of the proposed method and the traditional CA-based MBPU method.

The first experiment is performed on a simple simulated scenario, which has only two kind of height values (50 and 150 m). Fig. 5(a) is the reference DEM used in the simulation experiment. Fig. 5(b) and (c) are the simulated noisy interferograms of the short and long baselines (300 and 500 m), whose corresponding height ambiguities are 73.0 and 43.8 m, respectively. The mean coherence coefficient of Fig. 5(b) is 0.8 and that of Fig. 5(c) is 0.7. The probability density function of the noisy wrapped phase [42], [43] is used to simulate the phase noise. Obviously, since the height jump exceeds the height ambiguities of the two interferograms ($(150-50) > 73$ and $(150-50) > 43.8$), Fig. 5(b) and (c) cannot be unwrapped using the traditional SBPU technique. Therefore, only the MBPU technique can be used to solve this problem. After completing the 10 steps described in Section III-D, we can obtain the rest images of Fig. 5. Fig. 5(d) is the intercept obtained by the linear combination of Fig. 5(b) and (c) according to the first expression of (16). Fig. 5(e) is the corresponding histogram of Fig. 5(d). And Fig. 5(f) is the envelope of Fig. 5(e). From Fig. 5(e), we know

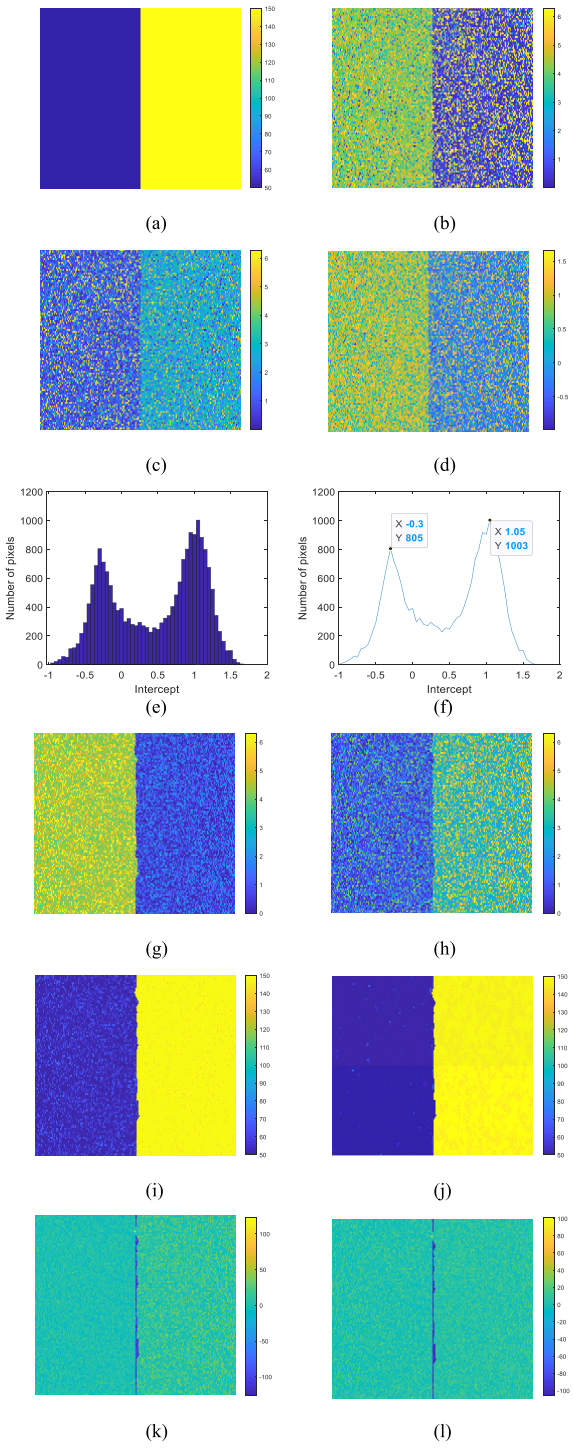

Fig. 5. (a) Reference DEM (unit: m). (b) Simulated interferogram for the short baseline. (c) Simulated interferogram for the long baseline. (d) Intercepts of all the pixels obtained by the linear combination of Fig. 5(b) and (c). (e) Histogram of the intercepts. (f) Envelop of the histogram. (g) Filtered interferogram for the short baseline. (h) Filtered interferogram for the long baseline. (i) Height reconstruction result before cluster filtering. (j) Height reconstruction result after cluster filtering. (k) Height error before cluster filtering. (l) Height error after cluster filtering.

that there are two effective clusters, and the intercepts of each cluster's centerline are -0.3 and 1.05, respectively, so their corresponding cluster intercepts are $-1/3$ and 1 according to the set S with $B_2/B_1 = \Gamma_1/\Gamma_2 = 5/3$. Then, if the

TABLE I
ERROR OF THE THREE EXPERIMENTS

		Mean height error	Std of height error	Normalized reconstruction square error
Experiment 1	Traditional CA-based method	5.80m	15.50m	0.022
	This paper's method	-3.10m	9.40m	0.013
Experiment 2	Baseline combination 1	-0.78m	8.95m	0.018
	Baseline combination 2	-2.37m	16.67m	0.062
Experiment 3	Traditional CA-based method	4.16m	7.48m	5.528×10^{-5}
	This paper's method	3.87m	4.93m	4.290×10^{-5}

traditional CA-based MBPU method is used, we need to search $5 \times 3 = 15$ times to determine the cluster ambiguity vector for each cluster, but only one time is needed when the closed-form solution formula (23) is used. Of course, the two cluster ambiguity vectors can also be determined by looking up the comparison table shown in Fig. 4, which are [2, 3] and [0, 1], respectively. Fig. 5(g) and (h) are the filtered interferograms of the short and long baselines after cluster phase filtering is completed. Compared with Fig. 5(b) and (c), the phase noise of Fig. 5(g) and (h) is obviously weakened, thereby verifying the effectiveness of cluster phase filtering. Fig. 5(i) and (j) are the DEM obtained by (1) before and after cluster phase filtering. In fact, Fig. 5(i) is the result obtained by the traditional CA-based MBPU method, and Fig. 5(j) is the result of the closed-form robust CA-based MBPUF method proposed in this article. Fig. 5(k) and (l) show the height errors of Fig. 5(i) and (j), respectively. The comparison of the experimental results based on the old and new methods is summarized in Table I. In Fig. 5(k), the mean value of the height errors is 5.80 m, the standard deviation is 15.50 m, and the normalized reconstruction square error, which is defined in [22] and [33], is 0.022. In contrast, the mean height error of Fig. 5(l) is -3.10 m, the standard deviation is 9.40 m, and the normalized reconstruction square error is 0.013. These experimental results show that the height accuracy is obviously improved after cluster phase filtering is completed, thereby verifying the feasibility and effectiveness of the closed-form robust CA-based MBPUF method proposed in this article.

In the second experiment, two different baseline combinations are tested on a more realistic scenario to verify the necessity of optimal baseline combination. The DEM of the mountainous area around the Isolation Peak (CO, USA) [5], as shown in Fig. 6(a), is used to simulate the interferograms. The minimum and maximum heights are 0 and 136.7 m, respectively. Assume that the search window size is $W_2 = 2$; it is known from (27) that the ratio between the long baseline and the short baseline must be greater than or equal to 3. Furthermore, according to the analysis of Section III-C, the total ambiguity height of each baseline combination must

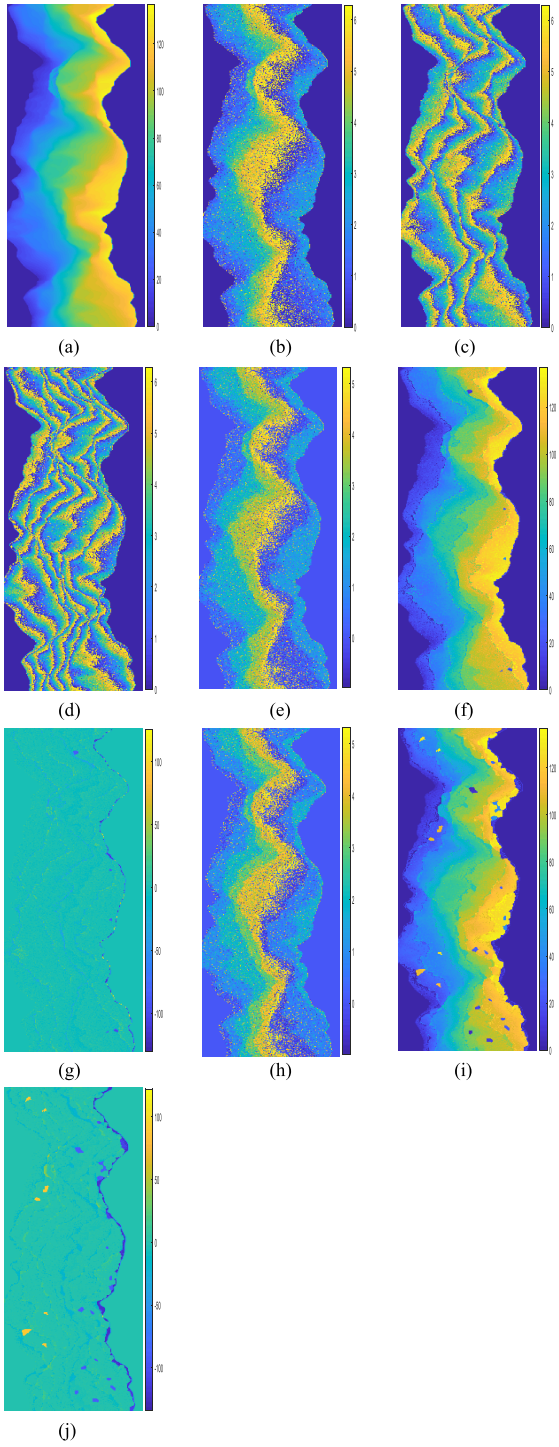

Fig. 6. DEM of the Isolation Peak, CO, USA, and the reconstructed results by the two different baseline combinations, 458 × 157 pixels. (a) Reference DEM (unit: m). (b) Simulated interferogram for baseline 1. (c) Simulated interferogram for baseline 2. (d) Simulated interferogram for baseline 3. (e) Intercepts of all the pixels obtained by the linear combination of Fig. 6(b) and (c). (f) Height reconstruction result using the combination of Fig. 6(b) and (c). (g) Height error of Fig. 6(f). (h) Intercepts of all the pixels obtained by the linear combination of Fig. 5(b) and (d). (i) Height reconstruction result using the combination of Fig. 6(b) and (d). (j) Height error of Fig. 6(i).

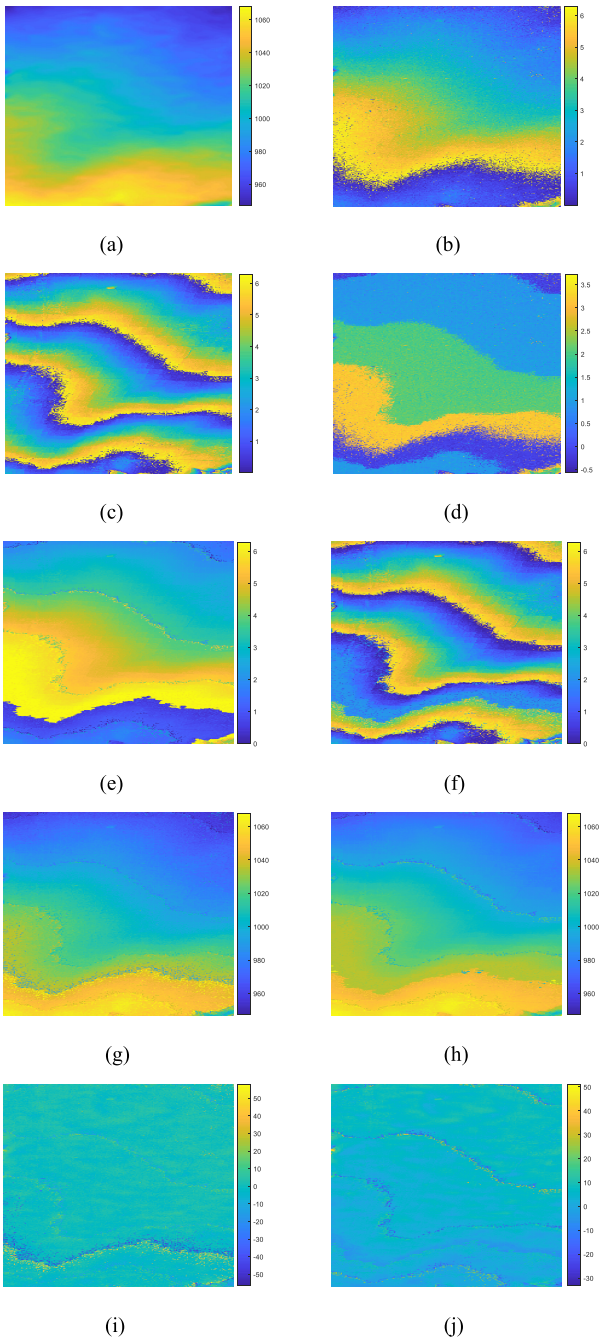

Fig. 7. Data set corresponds to a mountainous area in Tongchuan, Shaanxi Province, China, 736 × 191 pixels. (a) Reference SRTM DEM (unit: m). (b) Interferogram corresponding to the short baseline. (c) Interferogram corresponding to the long baseline. (d) Intercepts of all the pixels obtained by the linear combination of Fig. 7(b) and (c). (e) Filtered interferogram of the short baseline. (f) Filtered interferogram of the long baseline. (g) Height reconstruction result before cluster filtering. (h) Height reconstruction result after cluster filtering. (i) Height error of Fig. 7(g). (j) Height error of Fig. 7(h).

be greater than 136.7 m, and the length of B_2 should be as close as possible to B_1. Therefore, three noisy interferograms with three different baselines (60, 200, and 320 m) are simulated, as shown in Fig. 6(b)–(d). The corresponding height ambiguities are set to 93.0, 27.9, and 17.4 m, respectively, which make the length of any two baselines satisfy the condition (30). Fig. 6(b) and (c) form the first baseline combination ($B_2/B_1 = 10/3$) as the optimal baseline combination, and Fig. 6(b) and (d) form the second baseline combination ($B_2/B_1 = 16/3$) as the suboptimal baseline combination. The mean coherence coefficient of the three interferograms are all set to be 0.9 to compare the effects of different baseline combinations on the height-reconstruction results under the same phase noise. Fig. 6(e) is the intercept obtained by the linear combination of Fig. 6(b) and (c). The corresponding DEM-reconstruction result using the proposed closed-form robust CA-based MBPUF method is shown in Fig. 6(f), and Fig. 6(g) is the height error of Fig. 6(a)–(f). Fig. 6(h) is the intercept obtained by the linear combination of Fig. 6(b) and (d). Fig. 6(i) is the DEM-reconstruction result of the second baseline combination using the proposed closed-form robust CA-based MBPUF method. Fig. 6(j) shows the error between Fig. 6(a) and (i). A comparison of the two different baseline combinations is summarized in Table I. The comparison results are as follows: the mean height error of Fig. 6(f) is −0.78 m, the standard deviation is 8.95 m, and the normalized reconstruction square error is 0.018. On the contrary, the mean height error of Fig. 6(g) is −2.37 m, the standard deviation is 16.67 m, and the normalized reconstruction square error is 0.062. Obviously, based on these evaluation indicators, the DEM-reconstruction result of the first baseline combination is better than the second baseline combination. Therefore, we can conclude that under the preconditions that (27) and (30) are satisfied, the closer the length of the two baselines is, the more accurate the DEM-reconstruction result is. That is to say, this experiment verifies the reliability of optimal baseline combination in improving the noise robustness of the CA-based MBPU methods.

TABLE II
MAJOR PARAMETERS OF TANDEM-X INSAR DATA SET

	Interferogram 1		Interferogram 2	
	TDX-1	TSX-1	TDX-2	TSX-2
Incidence Angle	36.16°	36.07°	37.29°	37.05°
Acquisition Date	April 2 2014		October 21 2012	
Normal Baseline	129.25m		361.90m	
Range Pixel Spacing	5.45m			
Azimuth Pixel Spacing	8.15m			
Center Latitude	35.28°N			
Center Longitude	109.27°E			

In the third experiment, a real and small-scale single-pass TanDEM-X DB InSAR data set (736 × 191 pixels) is considered to evaluate the performance of the proposed method. The data set corresponds to a mountainous area in Tongchuan, Shaanxi Province, China. The other parameters about the data set are presented in Table II. Fig. 7(a) shows the reference Shuttle Radar Topography Mission (SRTM) DEM. Two single-pass InSAR interferograms with different baseline lengths are shown in Fig. 7(b) and (c), whose baseline lengths are 129.25 and 361.90 m, respectively. Fig. 7(d) shows the intercept obtained by the linear combination of Fig. 7(b) and (c). Fig. 7(e) and (f) are the filtered interferograms of the short and long baselines after the cluster phase filtering is applied. Fig. 7(g) and (h) are the DEM-reconstruction

results using the interferograms before and after the cluster phase filtering, which represent the results of the traditional CA-based MBPU method and the closed-form robust CA-based MBPUF method. Fig. 7(i) shows the error between Fig. 7(a) and (g). The comparison of the experimental results based on the old and new methods is summarized in Table I: the mean height error of Fig. 7(i) is 4.16 m, the standard deviation is 7.48 m, and the normalized reconstruction square error is 5.5280×10^{-5}. Fig. 7(j) shows the error between Fig. 7(a) and (h). The mean height error of Fig. 7(j) is 3.87 m, the standard deviation is 4.93 m, and the normalized reconstruction square error is 4.2900×10^{-5}. Therefore, the experimental results demonstrate the effectiveness of the proposed closed-form robust CA-based MBPUF method on the real InSAR data.

V. Conclusion

PU and phase filtering are the key procedures of the MB InSAR technique. To improve the performance of the CA-based MBPU methods, a closed-form robust CA-based MBPUF algorithm has been proposed in this article. The main contributions of this study are as follows. First, it gives the closed-form solving formulas of the cluster ambiguity vector, which is helpful to improve the efficiency of the CA-based MBPU algorithm. In addition, it provides a new MB InSAR phase-filtering strategy that makes the CA-based MBPU method capable of solving the phase-discontinuity problem and improving the height-reconstruction accuracy simultaneously. Moreover, it utilizes the optimal baseline combination to improve the noise robustness of the CA-based MBPU method. Three experiments with both simulated and real MB InSAR data sets are used to verify the effectiveness of the proposed method. It is worthwhile to mention that, all the three improvements proposed in this article for the CA-based MBPUF algorithm can also be used to improve the performance of the TSPAInSAR technique. Therefore, our future work should consider how to transplant the three improvements into the TSPAInSAR technique.

References

[1] T. Toutin and L. Gray, "State-of-the-art of elevation extraction from satellite SAR data," *ISPRS J. Photogramm. Remote Sens.*, vol. 55, no. 1, pp. 13–33, Nov. 2000.

[2] R. Bamler and P. Hartl, "Synthetic aperture radar interferometry," *Inverse Problems*, vol. 14, no. 4, pp. R1–R54, Aug. 1998.

[3] P. A. Rosen *et al.*, "Synthetic aperture radar interferometry," *Proc. IEEE*, vol. 88, no. 3, pp. 333–382, Mar. 2000.

[4] H. Yu, Y. Lan, Z. Yuan, J. Xu, and H. Lee, "Phase unwrapping in InSAR: A review," *IEEE Geosci. Remote Sens. Mag.*, vol. 7, no. 1, pp. 40–58, Mar. 2019.

[5] D. C. Ghiglia and M. D. Pritt, *Two-Dimensional Phase Unwrapping: Theory, Algorithms, and Software*. New York, NY, USA: Wiley, 1998.

[6] H. Yu, Y. Lan, J. Xu, D. An, and H. Lee, "Large-scale L^0 -norm and L^1 -norm 2-D phase unwrapping," *IEEE Trans. Geosci. Remote Sens.*, vol. 55, no. 8, pp. 4712–4728, Aug. 2017.

[7] H. Yu, M. Xing, and Z. Bao, "A fast phase unwrapping method for large-scale interferograms," *IEEE Trans. Geosci. Remote Sens.*, vol. 51, no. 7, pp. 4240–4248, Jul. 2013.

[8] K. Itoh, "Analysis of the phase unwrapping algorithm," *Appl. Opt.*, vol. 21, no. 14, p. 2470, 1982.

[9] W. Xu, E. C. Chang, L. K. Kwoh, H. Lim, W. Cheng, and A. Heng, "Phase-unwrapping of SAR interferogram with multi-frequency or multi-baseline," in *Proc. IEEE Int. Geosci. Remote Sens. Symp.*, Pasadena, CA, USA, Aug. 1994, pp. 730–732.

[10] M. Pinheiro, A. Reigber, R. Scheiber, P. Prats-Iraola, and A. Moreira, "Generation of highly accurate DEMs over flat areas by means of dual-frequency and dual-baseline airborne SAR interferometry," *IEEE Trans. Geosci. Remote Sens.*, vol. 56, no. 8, pp. 4361–4390, Aug. 2018.

[11] M. Lachaise, T. Fritz, and R. Bamler, "The dual-baseline phase unwrapping correction framework for the TanDEM-X mission Part 1: Theoretical description and algorithms," *IEEE Trans. Geosci. Remote Sens.*, vol. 56, no. 2, pp. 780–798, Feb. 2018.

[12] H. Yu, H. Lee, T. Yuan, and N. Cao, "A novel method for deformation estimation based on multibaseline InSAR phase unwrapping," *IEEE Trans. Geosci. Remote Sens.*, vol. 56, no. 9, pp. 5231–5243, Sep. 2018.

[13] P. Berardino, G. Fornaro, R. Lanari, and E. Sansosti, "A new algorithm for surface deformation monitoring based on small baseline differential SAR interferograms," *IEEE Trans. Geosci. Remote Sens.*, vol. 40, no. 11, pp. 2375–2383, Nov. 2002.

[14] T. R. Lauknes, H. A. Zebker, and Y. Larsen, "InSAR deformation time series using an L_1 -norm small-baseline approach," *IEEE Trans. Geosci. Remote Sens.*, vol. 49, no. 1, pp. 536–546, Jul. 2010.

[15] A. Ferretti, A. Fumagalli, F. Novali, C. Prati, F. Rocca, and A. Rucci, "A new algorithm for processing interferometric data-stacks: SqueeSAR," *IEEE Trans. Geosci. Remote Sens.*, vol. 49, no. 9, pp. 3460–3470, Sep. 2011.

[16] L. Zhang, X. Ding, and Z. Lu, "Ground deformation mapping by fusion of multi-temporal interferometric synthetic aperture radar images: A review," *Int. J. Image Data Fusion*, vol. 6, no. 4, pp. 289–313, Oct. 2015.

[17] D. C. Ghiglia and D. E. Wahl, "Interferometric synthetic aperture radar terrain elevation mapping from multiple observations," in *Proc. IEEE 6th Digit. Signal Process. Workshop*, Yosemite National Park, CA, USA, Oct. 1994, pp. 33–36.

[18] V. Pascazio and G. Schirinzi, "Estimation of terrain elevation by multi-frequency interferometric wide band SAR data," *IEEE Signal Process. Lett.*, vol. 8, no. 1, pp. 7–9, Jan. 2001.

[19] A. Ferretti, C. Prati, F. Rocca, and A. M. Guarnieri, "Multibaseline SAR interferometry for automatic DEM reconstruction," in *Proc. 3rd ERS Symp. Space Service Environ.*, Florence, Italy, 1997, pp. 1809–1820.

[20] A. Ferretti, C. Prati, and F. Rocca, "Multibaseline phase unwrapping for InSAR topography estimation," *Nuovo Cimento. C*, vol. 24, no. 1, pp. 159–176, Jan. 2001.

[21] G. Fornaro, A. Pauciullo, and E. Sansosti, "Phase difference-based multichannel phase unwrapping," *IEEE Trans. Image Process.*, vol. 14, no. 7, pp. 960–972, Jul. 2005.

[22] V. Pascazio and G. Schirinzi, "Multifrequency InSAR height reconstruction through maximum likelihood estimation of local planes parameters," *IEEE Trans. Image Process.*, vol. 11, no. 12, pp. 1478–1489, Dec. 2002.

[23] G. Ferraiuolo, V. Pascazio, and G. Schirinzi, "Maximum a posteriori estimation of height profiles in InSAR imaging," *IEEE Geosci. Remote Sens. Lett.*, vol. 1, no. 2, pp. 66–70, Apr. 2004.

[24] G. Ferraioli, A. Shabou, F. Tupin, and V. Pascazio, "Multichannel phase unwrapping with graph cuts," *IEEE Geosci. Remote Sens. Lett.*, vol. 6, no. 3, pp. 562–566, Jul. 2009.

[25] D. Chirico and G. Schirinzi, "Multichannel interferometric SAR phase unwrapping using extended Kalman smoother," *Int. J. Microw. Wireless Technol.*, vol. 5, pp. 429–436, Jun. 2013.

[26] R. Ambrosino, F. Baselice, G. Ferraioli, and G. Schirinzi, "Extended Kalman filter for multichannel InSAR height reconstruction," *IEEE Trans. Geos. Remote Sens.*, vol. 55, no. 10, pp. 5854–5863, Oct. 2017.

[27] G. Ferraioli, C.-A. Deledalle, L. Denis, and F. Tupin, "Parisar: Patch-based estimation and regularized inversion for multibaseline SAR interferometry," *IEEE Trans. Geosci. Remote Sens.*, vol. 56, no. 3, pp. 1626–1636, Mar. 2018.

[28] G. Ferraiuolo, F. Meglio, V. Pascazio, and G. Schirinzi, "DEM reconstruction accuracy in multichannel SAR interferometry," *IEEE Trans. Geosci. Remote Sens.*, vol. 47, no. 1, pp. 191–201, Jan. 2009.

[29] F. Baselice, G. Ferraioli, V. Pascazio, and G. Schirinzi, "Contextual information-based multichannel synthetic aperture radar interferometry: Addressing DEM reconstruction using contextual information," *IEEE Signal Process. Mag.*, vol. 31, no. 4, pp. 59–68, Jul. 2014.

[30] Y. F. Shao *et al.*, "Digital elevation model reconstruction in multichannel spaceborne/stationary SAR interferometry," *IEEE Geosci. Remote Sens. Lett.*, vol. 11, no. 12, pp. 2080–2084, Dec. 2014.

[31] A. E. Robertson, "Multi-baseline interferometric SAR for iterative height estimation," M.S. thesis, Dept. Elect. Comp. Eng., Brigham Young Univ., Provo, UT, USA, 1998.

[32] M. G. Kim and H. D. Griffiths, "Phase unwrapping of multibaseline interferometry using Kalman filtering," in *Proc. IET 7th Int. Conf. Image Process. Appl.*, Manchester, U.K., 1999, pp. 813–817.

[33] Z. Yuan, Y. Deng, F. Li, R. Wang, G. Liu, and X. Han, "Multichannel InSAR DEM reconstruction through improved closed-form robust chinese remainder theorem," *IEEE Geosci. Remote Sens. Lett.*, vol. 10, no. 6, pp. 1314–1318, Nov. 2013.
[34] H. Yu, Z. Li, and Z. Bao, "A cluster-analysis-based efficient multibaseline phase-unwrapping algorithm," *IEEE Trans. Geosci. Remote Sens.*, vol. 49, no. 1, pp. 478–487, Jan. 2011.
[35] H. Liu, M. Xing, and Z. Bao, "A cluster-analysis-based noise-robust phase-unwrapping algorithm for multibaseline interferograms," *IEEE Trans. Geosci. Remote Sens.*, vol. 53, no. 1, pp. 494–504, Jan. 2015.
[36] Z. Jiang, J. Wang, Q. Song, and Z. Zhou, "A refined cluster-analysis-based multibaseline phase-unwrapping algorithm," *IEEE Geosci. Remote Sens. Lett.*, vol. 14, no. 9, pp. 1565–1569, Sep. 2017.
[37] H. Yu and Y. Lan, "Robust two-dimensional phase unwrapping for multibaseline SAR Interferograms: A two-stage programming approach," *IEEE Trans. Geosci. Remote Sens.*, vol. 54, no. 9, pp. 5217–5225, Sep. 2016.
[38] Y. Lan, H. Yu, and M. Xing, "Refined two-stage programming-based multi-baseline phase unwrapping approach using local plane model," *Remote Sens.*, vol. 11, no. 5, p. 491, Feb. 2019.
[39] Y. Gao, S. Zhang, T. Li, Q. Chen, X. Zhang, and S. Li, "Refined two-stage programming approach of phase unwrapping for multi-baseline SAR interferograms using the unscented Kalman filter," *Remote Sens.*, vol. 11, p. 199, Jan. 2019.
[40] L. Zhou, D. Chai, Y. Xia, and C. Xie, "An extended PUMA algorithm for multibaseline InSAR DEM reconstruction," *Int. J. Remote Sens.*, vol. 40, no. 20, pp. 7830–7851, 2019.
[41] H. Yu, Y. Zhou, S. S. Ivey, and Y. Lan, "Large-scale multibaseline phase unwrapping: Interferogram segmentation based on multibaseline envelope-sparsity theorem," *IEEE Trans. Geosci. Remote Sens.*, vol. 57, no. 11, pp. 9308–9322, Nov. 2019.
[42] D. Just and R. Bamler, "Phase statistics of interferograms with applications to synthetic aperture radar," *Appl. Opt.*, vol. 33, no. 20, pp. 4361–4368, 1994.
[43] J.-S. Lee, K. W. Hoppel, S. A. Mango, and A. R. Miller, "Intensity and phase statistics of multilook polarimetric and interferometric SAR imagery," *IEEE Trans. Geosci. Remote Sens.*, vol. 32, no. 5, pp. 1017–1028, Sep. 1994.
[44] X. Xianming and P. Yiming, "Multi-baseline phase unwrapping algorithm based on the unscented Kalman filter," *IET Radar, Sonar Navigat.*, vol. 5, no. 3, pp. 296–304, 2011.
[45] B. Osmanoğlu, T. H. Dixon, and S. Wdowinski, "Three-dimensional phase unwrapping for satellite radar interferometry, I: DEM generation," *IEEE Trans. Geosci. Remote Sens.*, vol. 52, no. 2, pp. 1059–1075, Feb. 2014.
[46] X. Zhang, Q. Zeng, J. Jiao, and J. Zhang, "Fusion of space-borne multibaseline and multi-frequency interferometric results based on extended Kalman filter to generate high quality DEMs," *ISPRS J. Photogramm. Remote Sens.*, vol. 111, pp. 32–44, Jan. 2016.
[47] H. Yu, H. Lee, N. Cao, and Y. Lan, "Optimal baseline design for multibaseline InSAR Phase unwrapping," *IEEE Trans. Geosci. Remote Sens.*, vol. 57, no. 8, pp. 5738–5750, Aug. 2019.
[48] W. Wang and X.-G. Xia, "A closed-form robust Chinese remainder theorem and its performance analysis," *IEEE Trans. Signal Process.*, vol. 58, no. 11, pp. 5655–5666, Nov. 2010.

Zhihui Yuan (Member, IEEE) was born in Hunan, China, in 1983. He received the B.S. degree in electronic information engineering from Xiangtan University, Xiangtan, China, in 2007, and the Ph.D. degree in communication and information systems from the Institute of Electronics, Chinese Academy of Sciences, Beijing, China, in 2013.

Since 2013, he has been a Lecturer with the School of Electrical and Information Engineering, Changsha University of Science and Technology, Changsha, China. From 2018 to 2019, he was a Visiting Scholar with the Roy M. Huffington Department of Earth Sciences, Southern Methodist University, Dallas, TX, USA, working with Prof. Z. Lu on the interferometric synthetic aperture radar (InSAR) technique. He is also a Principal Investigator of the scientific project Research on Multichannel InSAR Robust DEM Inversion With High Precision for Complicated Terrain supported by the National Natural Science Foundation of China. His research interests include signal processing and the application of synthetic aperture radar interferometry, phase unwrapping, high-resolution digital elevation model generation, and algorithm design.

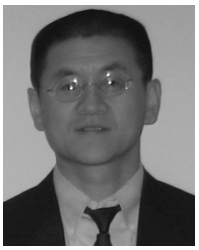

Zhong Lu (Senior Member, IEEE) received the B.S. and M.S. degrees from Peking University, Beijing, China, in 1989 and 1992, respectively, and the Ph.D. degree from the University of Alaska Fairbanks, Fairbanks, AK, USA, in 1996.

He was a Physical Scientist with the U.S. Geological Survey (USGS), Reston, VA, USA, from 1997 to 2013. He is currently a Professor and the Endowed Shuler-Foscue Chair with the Roy M. Huffington Department of Earth Sciences, Southern Methodist University, Dallas, TX, USA. He is also a Principal Investigator of projects funded by NASA, ESA, JAXA, DLR, and USGS on the study of land surface deformation using the satellite interferometric synthetic aperture radar (InSAR) imagery. He has authored or coauthored over 190 peer-reviewed journal articles and book chapters focused on InSAR techniques and applications. He has authored the book, *InSAR Imaging of Aleutian Volcanoes: Monitoring a Volcanic Arc From Space* (Springer, 2014). His research interests include technique developments of SAR, InSAR, and persistent scatterer InSAR processing and their applications on natural hazard monitoring and natural resource characterization.

Dr. Lu is a Committee Member of the International User Team for Radarsat-C SAR Constellations, the Geo Earth Scope InSAR User Working Group, the NASA's Alaska Satellite Facility User Working Group, and the upcoming NASA-India SAR Science Team. He is also a member of the Editorial Boards of the *International Journal of Image* and *Data Fusion and Geomatics, Natural Hazards and Risk.* He was a recipient of the Ford Senior Research Fellowship, the Science of Risk Prize, the American Society for Photogrammetry and Remote Sensing Award for the Best Scientific Paper in Remote Sensing, the NASA Group Achievement Award, the NASA Certificate of Appreciation, the Raytheon Distinguished Level Award for Excellence in Technology, Science Applications, International Corporation Technical Fellow, and the Jerald Cook Memorial Award. He is the Chair of the Western North America InSAR Consortium. He is a Senior Associate Editor of *Remote Sensing* and an Associate Editor of *Frontiers in Volcanology.*

Lifu Chen was born in 1979. He received the B.S. degree in electronic information engineering from Beihang University, Beijing, China, in 2007, and the Ph.D. degree in communication and information systems from the Institute of Electronics, Chinese Academy of Sciences, Beijing, in 2011.

Since 2011, he has been a Lecturer with the School of Electrical and Information Engineering, Changsha University of Science and Technology, Changsha, China. From August 2018 to August 2019, he was a Visiting Scholar with the School of Engineering, Newcastle University, Newcastle upon Tyne, U.K., working with Prof. Z. Li on AI in synthetic aperture radar (SAR)/interferometric SAR (InSAR) images. He is a Principal Investigator of the Scientific Project Research on Real-Time DEM Reconstruction With High Precision Using Airborne InSAR System supported by the National Natural Science Foundation of China. He has authored more than 40 articles. His research interests include SAR/InSAR signal processing, targets detection, and terrain classification for SAR/InSAR image with deep learning (landslide detection, classification for remote sensing images, extraction of water, and shadow and layover from InSAR images).

Xuemin Xing was born in Liaoning, China, in 1983. She received the B.S. and M.S. degrees and the Ph.D. degree in geomatics and surveying from Central South University, Changsha, China, in 2005, 2008, and 2011, respectively.

From 2016 to 2017, she was a Visiting Scholar with the Department of Environmental Sciences, Macquarie University, Sydney, NSW, Australia. She is currently an Associate Professor with the School of Traffic and Transportation Engineering, Changsha University of Science and Technology, Changsha, where she is also a Key Member of the Laboratory of Radar Remote Sensing Applications. She is also a reviewer for three international journals and four national journals in China. She has authored more than 20 articles and 3 inventions. Her research interest includes the application of time-series interferometric synthetic aperture radar (InSAR) technique in highway deformation monitoring, deriving spatial–temporal large-scale deformation induced by mining activities and modeling, and the integration of persistent scatterer (PS), corner reflector (CR), and small baseline subset (SBAS) technique.